Supplementary Materials

Fast three-dimensional nanoimaging of electron-beam-sensitive metal-organic frameworks-encapsulated materials

Ke Ma[1], Lipei Yu[1], Bangchao Wang[1], Jiangtao Zhu[1], Shiqiang Feng[1,2], Lili Han[1]

[1]State Key Laboratory of Structural Chemistry, Fujian Institute of Research on the Structure of Matter, Chinese Academy of Sciences, Fuzhou 350002, Fujian, China.
[2]Fujian Science & Technology Innovation Laboratory for Optoelectronic Information of China, Fuzhou 350108, Fujian, China.

Correspondence to: Prof. Lili Han, State Key Laboratory of Structural Chemistry, Fujian Institute of Research on the Structure of Matter, Chinese Academy of Sciences, Fuzhou 350002, Fujian, China. E-mail: llhan@fjirsm.ac.cn; Dr. Shiqiang Feng, State Key Laboratory of Structural Chemistry, Fujian Institute of Research on the Structure of Matter, Chinese Academy of Sciences, Fuzhou 350002, Fujian, China; Fujian Science & Technology Innovation Laboratory for Optoelectronic Information of China, Fuzhou 350108, Fujian, China. E-mail: fengshiqiang@fjirsm.ac.cn

Comparison of fast and conventional acquisition

To further validate the practical efficacy of the pre-calibration method, we acquired two repeat tilt series using conventional and pre-calibration fast acquisition approaches. The Pt-Zn alloy nanoparticles supported on graphene oxide (GO) is served as test sample, which exhibits sufficient resistance to repeated electron beam irradiation. A 200-nm margin is reserved on all sides of the acquisition window to prevent sample drift out of the imaging area. A rigid intensity-based registration algorithm automatically aligns the fast-acquisition projections with the conventional images (used as reference) and records the rigid offset values, as shown in Supplementary Figure 4a and b and Supplementary Figure 5. The results indicate that the maximum translation distance measures 131.5 nm (below the 200 nm safety threshold), demonstrating the efficacy of the automated specimen tracking system.

Having validated the effectiveness of specimen tracking, a comprehensive assessment of image quality was conducted, where the sharpness of images serves as a critical indicator of proper focus during fast acquisition. By calculating the variance of Laplacian (VOL) and high-frequency ratio (HFR) of both image datasets, we performed a no-reference image sharpness assessment, as shown in Supplementary Figure 4 c and d. The results demonstrate marginally lower sharpness in fast-acquisition images compared to conventional acquisition (VOL: 1.425±0.131 vs 1.385±0.289; HFR: 0.241±0.010 vs 0.226±0.024). This sharpness reduction is better than the effect of Gaussian filtering (σ=0.4 kernel) applied to conventional-acquisition images (VOL: 1.103, HFR: 0.215), confirming that the fast-acquisition method maintains sufficient image sharpness with proper focus during capture. In addition, we supplemented the analysis of SSIM and PSNR to quantitatively assess the preservation of structural information and image signal-to-noise ratio of fast-acquisition images (Supplementary Figure 4e andf). The results indicate that SSIM values of fast-acquisition images predominantly exceed 0.9, with a mean of 0.949±0.013, demonstrating high structural similarity to reference images. Concurrently, PSNR of tilt series surpasses 33 dB (mean: 35.08±1.07 dB), confirming excellent imaging clarity and sufficient signal quality. Comprehensive evaluation using multiple image quality metrics (VOL: 1.385, HFR: 0.226, SSIM: 0.949±0.013, PSNR: 35.08±1.07 dB) confirms excellent quality in fast-acquisition images, demonstrating both proper defocus and sufficient exposure time during acquisition.

The same pre-processing procedure are employed on both tilt series, including image denoising, image alignment and tilt axis alignment, and applied 3D reconstruction using 50 cycles simultaneous iterative reconstruction technique (SIRT). The volumetric views of the 3D reconstructions demonstrate high similarity of two methods, with no observable structural discrepancies (Supplementary Figure 4g). Following intensity normalization and spatial alignment of the two 3D volumes, the structural fidelity of the fast-acquisition volume is quantified by 3D mean absolute error (MAE_{3D}), 3D root mean square error ($RMSE_{3D}$) and $SSIM_{3D}$, with a reference of convention-acquisition volume. The results demonstrated excellent agreement: (i) MAE_{3D} = 0.0029 (values <0.005 indicate negligible structural differences). (ii) $RMSE_{3D}$ = 0.0064 (values <0.02 suggest minimal structural variance). (iii) $SSIM_{3D}$ = 0.962±0.023 (values >0.9 denote no observable structural discrepancies).

MNPs@ZIF-8 Series Acquisition

We implement fast ET for tilt-series acquisition, incorporating a pre-calibration step on near carbon films with 8° tilt increments to record image shift and defocus parameters. During data acquisition, an 8-second exposure time per image is set with 2-second relaxation intervals to minimize sample drift. The electron beam is maintained in "beam blank" mode during both stage tilting and relaxation periods to reduce accumulated electron dose. Furthermore, the system permits temporary pauses for manual fine-tuning when excessive drift is detected.

Supplementary Table 1. Dose estimation of conventional and rapid ET acquisition methods for MNPs@ZIF-8 sample

Step	Convention	Rapid
Acquisition	Beam current: 50 pA	Beam current:50 pA
	Dwell time: 30 µs	Dwell: 30 µs
	Pixel size: 2500 pm	Pixel size: 2500 pm
	Frame time: 8 s	Frame time: 8 s
	Frame size: 512	Frame size: 512
	# frames: 66	# frames: 66
Dose(e/Å^2)	988.7	988.7
Time (s)	528	528
Tracking & Focus	Beam current: 50 pA	-
	Dwell time: 12 µs	
	Frame time: 3 s	
	Frame size: 512	
	Pixel size: 2500 pm	
	# frames: 66*20	
Dose(e/Å^2)	$7.91*10^3$	
Time (s)	3960	
Tilting time (s)	66	66
Total dose (e/Å^2)	$8.90*10^3$	988.7
Total time (s)	4554	594

Electron dose is calculated as:

$$Dose = \frac{beam\ current \times dwell\ time}{electron\ charge \times pixel\ size^2} \times number\ of\ frames$$

Implementation of the pre-calibration method achieved an 88.9% reduction in cumulative electron dose exposure.

Supplementary Table 2. Parameters for Box-Plot of x-shifts error

Group	***Lower (nm)***	***Q1 (nm)***	***Q2 (nm)***	***Q3 (nm)***	***Upper (nm)***
A1	-66.4	-22.3	-6.2	8.5	48.2
A2	-43.2	-25.4	-4.8	5.6	20.1
A3	-50.5	-30.3	-4.4	16	62.5
B	-48.2	-18.5	12.0	34.7	109.6
C	-134.4	-69.3	-22.3	50.1	119.2

Group A1 contained outliers at -106.7 nm, -78.7 nm and 72.4 nm, while no outliers are detected in the other groups.

Supplementary Table 3. Parameters for Box-Plot of y-shifts error.

Group	***Lower (nm)***	***Q1 (nm)***	***Q2 (nm)***	***Q3 (nm)***	***Upper (nm)***
A1	-87.3	-43.1	-24.2	-5.2	4.6
A2	-138.0	-53.3	-1.6	13.6	68.7
A3	-166.9	-52.8	2.2	31.6	48.4
B	-66.6	-37.7	-7.8	64.0	129.0
C	-419.5	-196.7	-5.4	134.5	206.2

No outliers were detected in any groups.

Supplementary Table 4. Parameters for Box-Plot of defocus error

Group	***Lower (nm)***	***Q1 (nm)***	***Q2 (nm)***	***Q3 (nm)***	***Upper (nm)***
A1	-119.7	-48.0	-6.3	37.4	129.5
A2	-169.5	-86.0	-50.1	-28.3	54.3

A3	-102.7	-15.8	15.8	77.0	139.7
B	-167.9	-120.2	-56.8	-11.6	115.9
C	-263.7	-121.9	-30.8	125.6	281.5

No outliers were detected in any groups.

Supplementary Table 5. Synthesis parameters of MNPs@ZIF-8

Name	MNPs type	Time (h)	NPs amount (ml)	Extra PVP	Zn^{2+}: ligand
Reference	Au	24	1.0	0	1:1
Pd	Pd	24	1.0	0	1:1
Time	Au	48	1.0	0	1:1
mMNPs1	Au	24	1.15	0	1:1
mMNPs2	Au	24	2.0	0	1:1
Ratio	Au	24	1.0	0	6:5
mPVP1	Au	24	1.0	1×10^{-4} wt.%	1:1
mPVP2	Au	24	1.0	5×10^{-4} wt.%	1:1

Supplementary Table 6. Fitting parameters and error estimates for the exponential decay model of radial distribution

Name	A	k	RMSE	R-square
Reference	1.43	0.0149	0.04	0.94
Pd	3.68	0.0229	0.02	0.99
Time	2.70	0.0183	0.05	0.95
mMNPs1	3.41	0.0197	0.02	0.99
mMNPs2	1.09	0.0068	0.07	0.91
Ratio	1.08	0.0063	0.07	0.90
mPVP1	0.25	0.0041	0.04	0.63
mPVP2	0.21	0.0048	0.03	0.68

Standard exponential decay model takes the form:

$$r_d(r) = A \cdot e^{-k \cdot r}$$

where r is represents the radial distance of MNPs, r_d is the normalized density of MNPs for each shell layer, A is the initial amplitude, and k is accounts for the decay rate. The fitting accuracy was evaluated using both root-mean-square error (RMSE) and R-square. The relatively low R^2 values (0.63-0.91) for the last four samples indicate inadequate adaptability of the fitting function to these datasets.

Supplementary Table 7. Fitting parameters and error estimates for the "plateau + exponential decay" model of radial distribution (RD)

Name	D	r_0 (nm)	k	RMSE	R-square
mMNPs2	0.56	151.28	0.0116	0.03	0.98
Ratio	0.55	175.41	0.0124	0.04	0.97
mPVP1	0.15	280.71	0.0207	0.02	0.89
mPVP2	0.11	279.24	0.0276	0.02	0.85

Standard "plateau + exponential decay" model takes the form:

$$r_d(r) = \begin{cases} D, r \leq r_0 \\ D \cdot e^{-k(r-r_0)}, r \geq r_0 \end{cases}$$

where r is represents the radial distance of MNPs, r_d is the normalized density of MNPs for each shell layer, D is the plateau magnitude, r_0 is the radical distance of plateau, and k is accounts for the decay rate. The piecewise "plateau + exponential decay" function demonstrates superior R-square values, indicating the existence of a saturation region in the radial distribution of MNPs.

Supplementary Table 8. Fitting parameters and error estimates for the Gaussian model of MNPs nearest neighbor distance

Name	***A***	**μ (nm)**	**σ (nm)**	**FWHM (nm)**	**R-square**
Reference	0.1025	23.74	3.64	8.58	0.98
Pd	0.0993	23.84	3.84	9.04	0.99
Time	0.1054	23.51	3.70	8.70	0.99
mMNPs1	0.1036	22.44	3.62	8.52	0.98
mMNPs2	0.0932	23.35	4.11	9.68	0.99
Ratio	0.0974	23.31	3.82	9.01	0.98

mPVP1	0.0480	26.03	7.04	16.59	0.84
mPVP2	0.0304	36.57	13.85	32.60	0.84

Standard exponential decay model takes the form:

$$f(x) = A \cdot e^{-\frac{(x-\mu)^2}{2\sigma^2}}$$

Where A is the amplitude or peak height, μ is the mean value or peak position, σ is the standard deviation, FWHM is the full width at half maximum, and R-square represents the coefficient of determination. PVP-modified samples exhibited distinct peak shifts and significant broadening of the FWHM, indicating both improved MNPs dispersion and increased distribution heterogeneity.

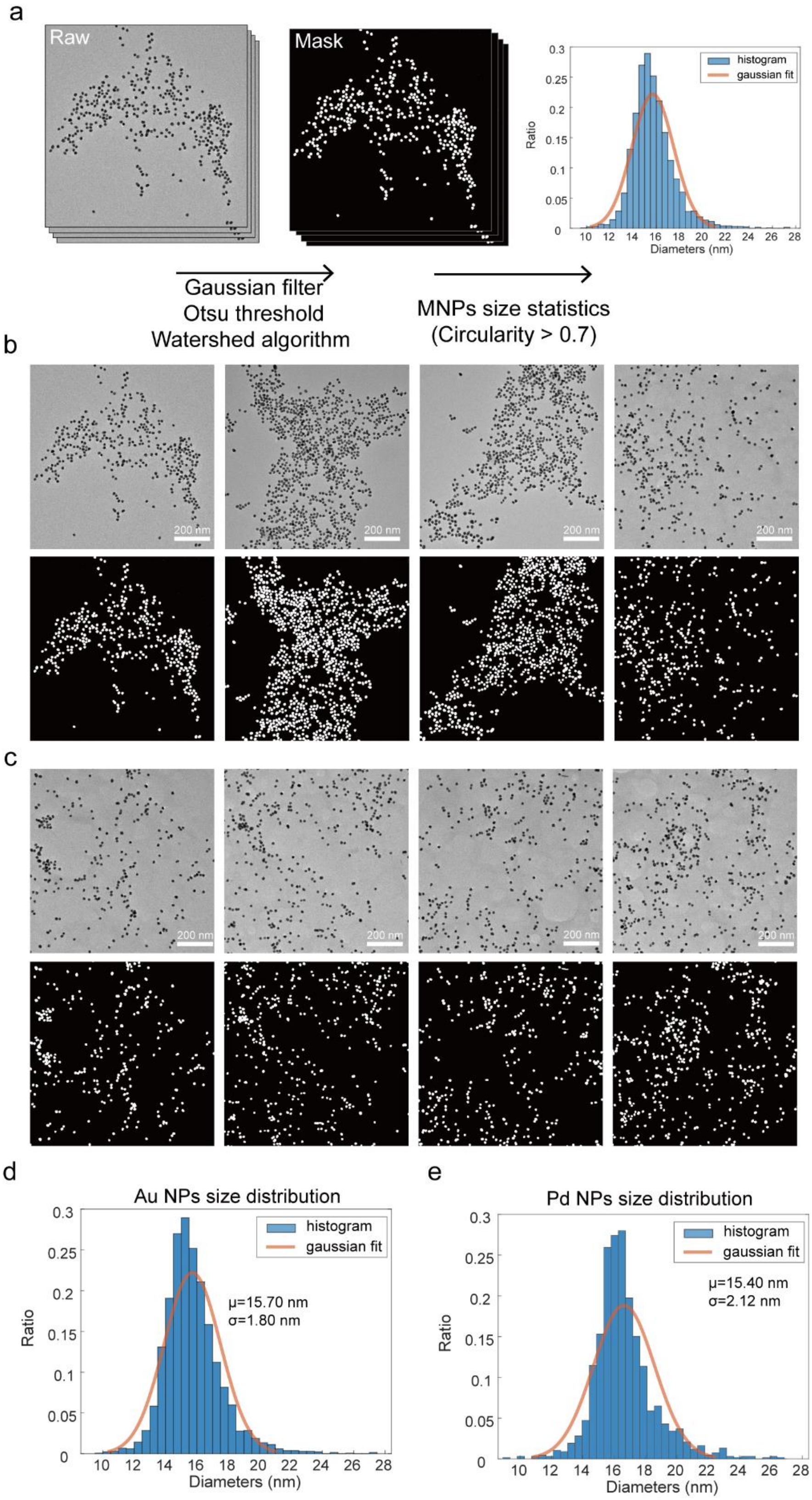

Supplementary Figure 1. Size distribution calculation. a) Size distribution calculation workflow. b,c) TEM images and mask of Au NPs and Pd NPs, respectively. d,e) Size distribution of Au NPs and Pd NPs.

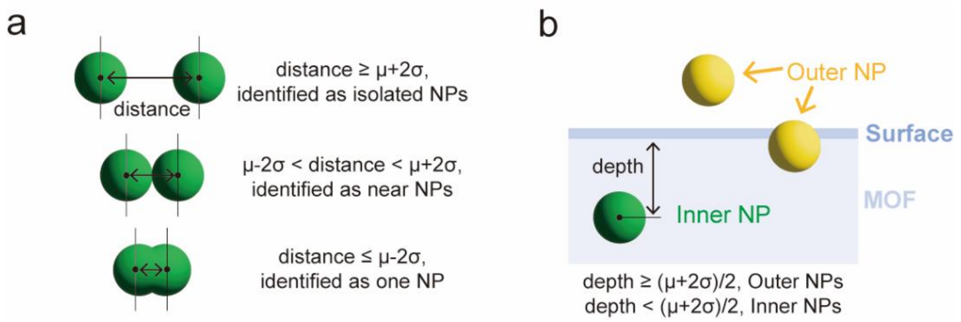

Supplementary Figure 2. Determination of aggregation and encapsulation. a) Determination of MNPs aggregation. b) Determination of MNPs encapsulation.

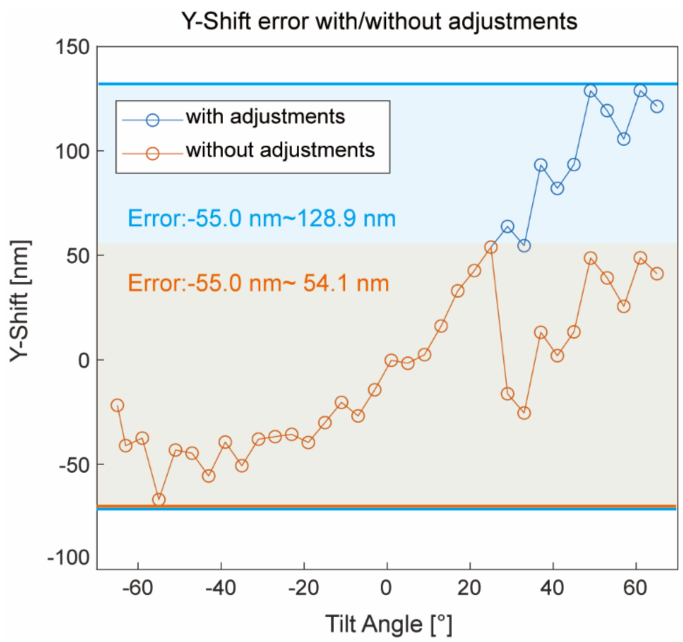

Supplementary Figure 3. Comparison of image shift errors with/without adjustments.

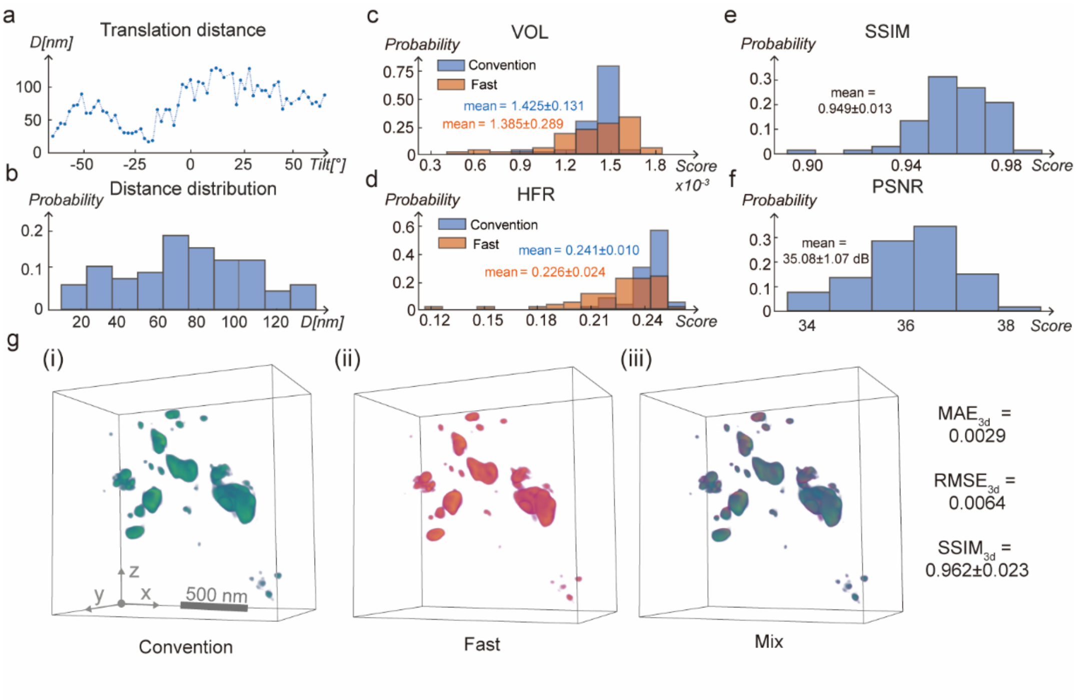

Supplementary Figure 4. Comparison of actual acquisition results from rapid versus conventional methods. a-b) Image translation condition and its distribution. c-d) VOL and HFR metrics of tilt series from convention/rapid methods. e-f) SSIM and PSNR of rapid-acquisition series comparing convention-acquisition method. g) Visualization and quantification of differences in reconstructions.

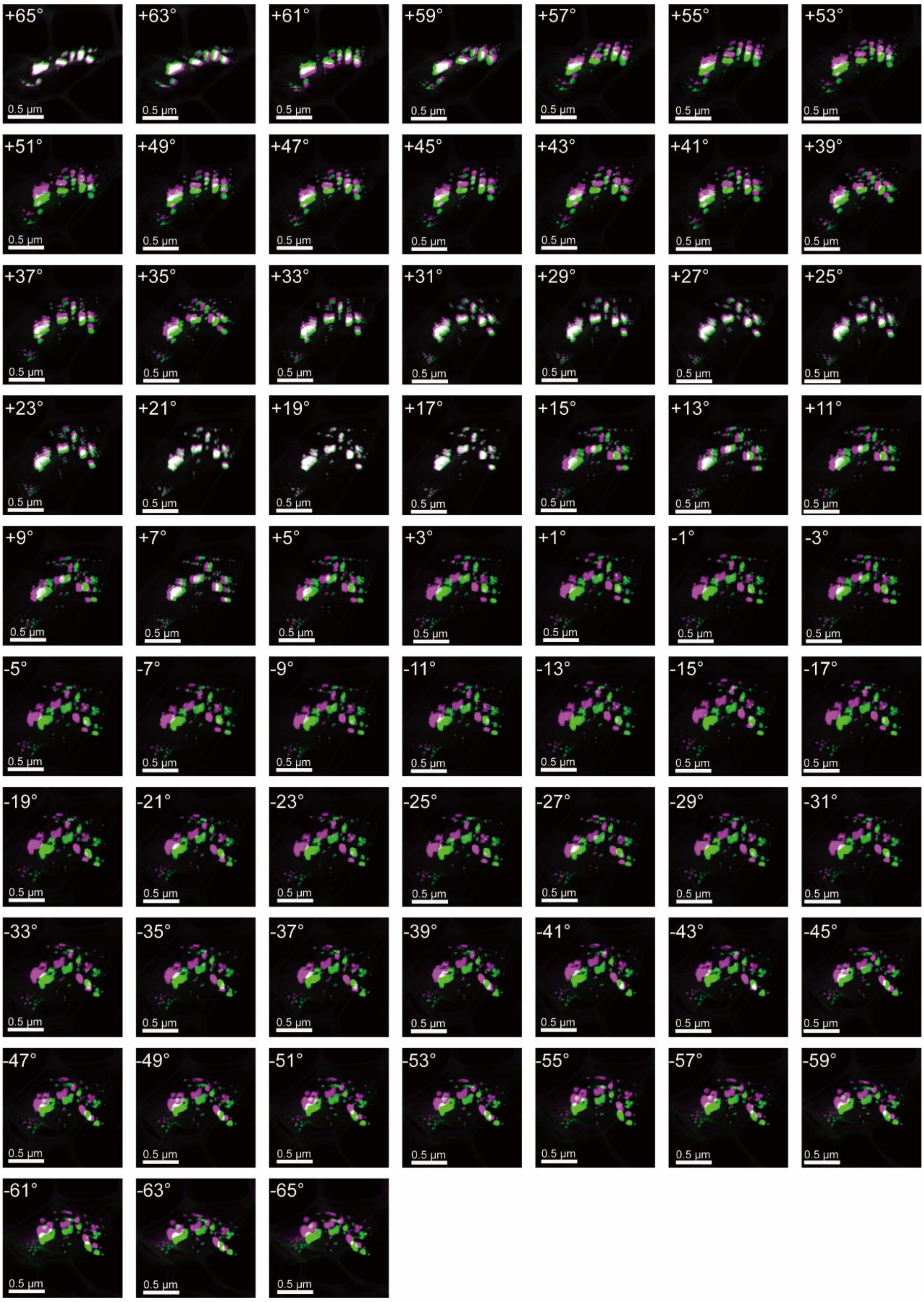

Supplementary Figure 5. Differential map of tilt series acquired by rapid/conventional-acquisition method. Using conventional acquisition images as the reference, differential map displays intensity-deficient regions in red, intensity-enhanced regions in green, and intensity-overlapping areas in white for the rapid-acquisition images.

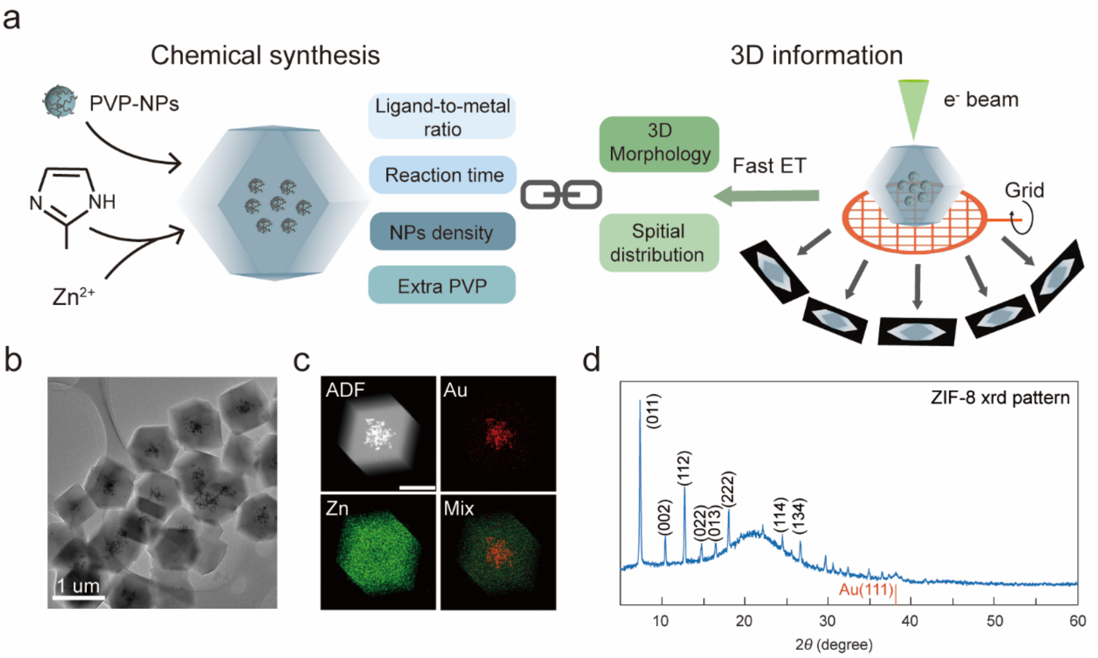

Supplementary Figure 6. Research outline and basic characterization. a) Investigation strategy for rapid ET of MNPs@ZIF-8. b-d) TEM, EDS-mapping and XRD characterization of standard Au NPs@ZIF-8, respectively.

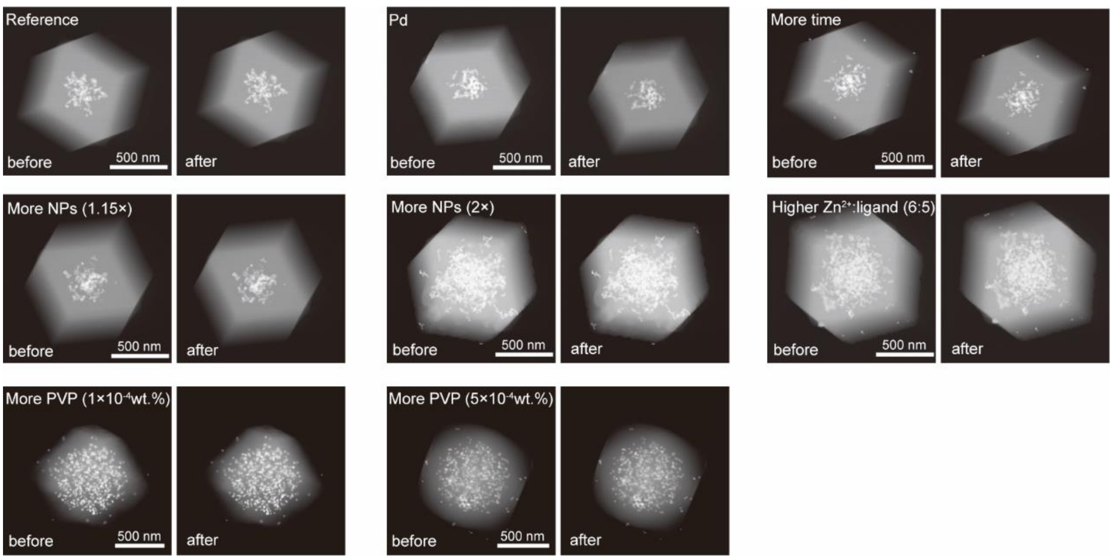

Supplementary Figure 7. 0° projections before and after rapid ET acquisition across different samples. No structural damage is detected.

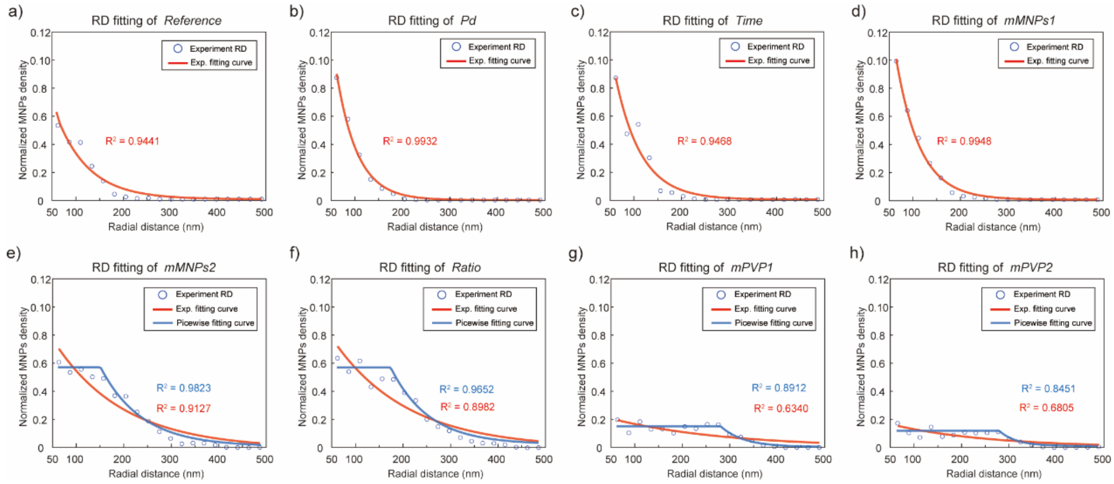

Supplementary Figure 8. MNPs radial distributions and corresponding fitting curves. R-square values for exponential decay model (red) and plateau + exponential decay model (blue) inserted in the figures.

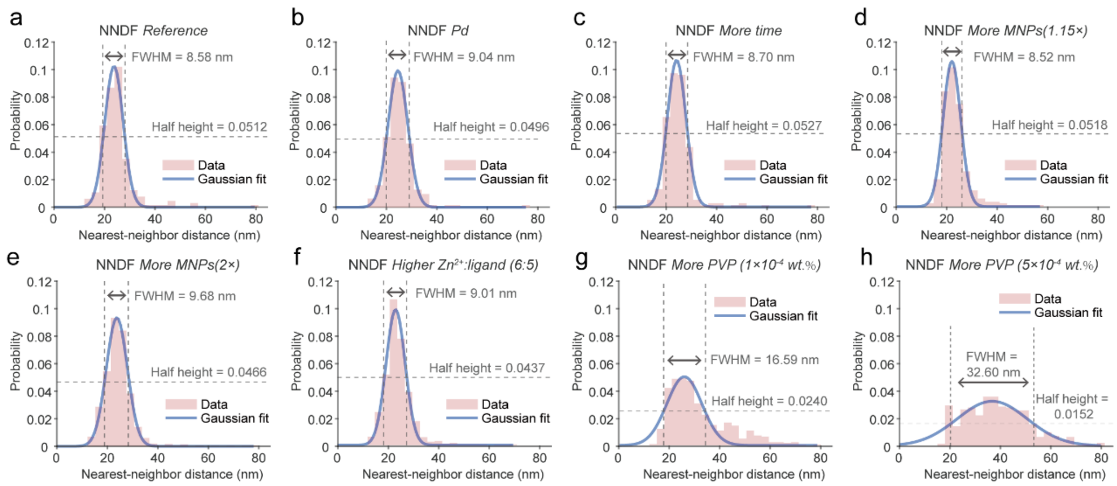

Supplementary Figure 9. MNPs nearest-neighbor distances and corresponding Gaussian fitting curves. FWHM and half-peak height are inserted in figures. Samples with extra PVP addition shows higher dispersion disorder.